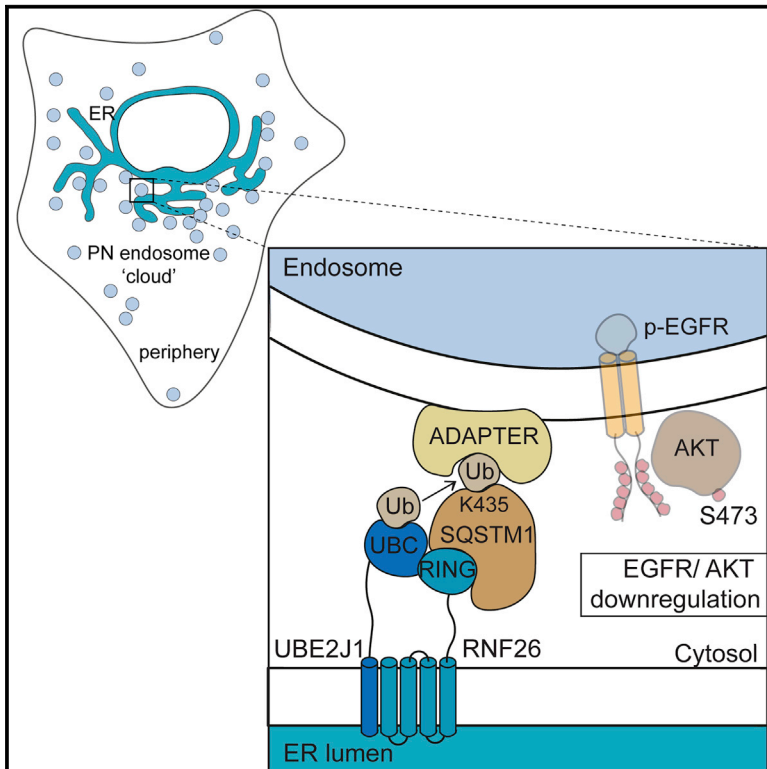**Article**

The ER-embedded UBE2J1/RNF26 ubiquitylation complex exerts spatiotemporal control over the endolysosomal pathway

Graphical Abstract

Authors

Tom Cremer, Marlieke L.M. Jongsma, Fredrik Trulsson, Alfred C.O. Vertegaal, Jacques Neefjes, Ilana Berlin

Correspondence

j.j.c.neefjes@lumc.nl (J.N.),
i.berlin@lumc.nl (I.B.)

In Brief

Cremer et al. identify UBE2J1 as the E2 partner for RNF26 in the spatiotemporal organization of endosomes and lysosomes, accomplished through the ubiquitylation of SQSTM1 on lysine 435. Together, these ER-associated enzymes promote the timely downregulation of EGFR and downstream Akt signaling.

Highlights

- UBE2J1 supports RNF26-mediated perinuclear organization of the endolysosomal system

- UBE2J1/RNF26 complex formation is supported by transmembrane interactions

- UBE2J1/RNF26 complex ubiquitinates SQSTM1 on lysine 435

- UBE2J1/RNF26-dependent endosomal organization promotes downregulation of EGFR/Akt

CellPress

Article

The ER-embedded UBE2J1/RNF26 ubiquitylation complex exerts spatiotemporal control over the endolysosomal pathway

Tom Cremer,[1] Marlieke L.M. Jongsma,[1,2] Fredrik Trulsson,[1,2] Alfred C.O. Vertegaal,[1,3] Jacques Neefjes,[1,3,*] and Ilana Berlin[1,3,4,*]

[1]Department of Cell and Chemical Biology, Leiden University Medical Center (LUMC), Einthovenweg 20, 2300RC Leiden, the Netherlands
[2]These authors contributed equally
[3]Senior authors
[4]Lead contact
*Correspondence: j.j.c.neefjes@lumc.nl (J.N.), i.berlin@lumc.nl (I.B.)
https://doi.org/10.1016/j.celrep.2020.108659

SUMMARY

The endolysosomal system fulfills a wide variety of cellular functions, many of which are modulated through interactions with other organelles. In particular, the ER exerts spatiotemporal constraints on the organization and motility of endosomes and lysosomes. We have recently described the ER transmembrane E3 ubiquitin ligase RNF26 as a regulator of endolysosomal perinuclear positioning and transport dynamics. Here, we report that the ubiquitin conjugating enzyme UBE2J1, also anchored in the ER membrane, partners with RNF26 in this context, and that the cellular activity of the resulting E2/E3 pair is localized in a perinuclear ER subdomain and supported by transmembrane interactions. Through modification of SQSTM1/p62 on lysine 435, the ER-embedded UBE2J1/RNF26 ubiquitylation complex recruits endosomal adaptors to immobilize their cognate vesicles in the perinuclear region of the cell. The resulting spatiotemporal compartmentalization promotes the trafficking of activated EGFR to lysosomes and facilitates the termination of EGF-induced AKT signaling.

INTRODUCTION

Eukaryotic cells have evolved a complex architecture encompassing the nucleus, cytoplasm, and various specialized organelles, all confined within a small three-dimensional (3D) space. While compartmentalization enables cells to maintain order, interactions between compartments in turn offer opportunities for integration and co-regulation of essential cellular processes. For instance, the endoplasmic reticulum (ER), typically the largest organelle of the cell, offers an excellent platform for the regulation of smaller intracellular structures. In fact, membrane contact sites (MCSs) between the ER and virtually every intracellular organelle have been reported to date, allowing controlled exchanges of information and materials to occur between them (Phillips and Voeltz, 2016; Wong et al., 2019). Uncovering ways in which the ER communicates with and influences other organelles is crucial to our understanding of how cells coordinate their internal affairs and respond to their environment.

The endolysosomal system, comprising a vesicular network whose members are both physically independent and functionally interconnected, presents a unique case in its relationship with the ER (Raiborg et al., 2015b). The endocytic compartment fulfills a wide variety of cellular roles, ranging from the regulation of signaling and proteostasis (Di Fiore and von Zastrow,

2014; Khaminets et al., 2016) to control of cell polarity (Jewett and Prekeris, 2018), migration (Malinova and Huveneers, 2018; Paul et al., 2015), defense against pathogenic invaders (Taguchi and Mukai, 2019), and communication between cells (Maas et al., 2017). Once nascent endosomes bud inward from the plasma membrane, engulfing extracellular milieu, they embark on a journey of maturation, guided in part by the ER (Bakker et al., 2017). Traveling deeper into the cell interior, endosomes progressively acquire late characteristics of acidity and proteolytic potential (Huotari and Helenius, 2011) and engage in more frequent and persistent contacts with the ER membrane. These interactions have been shown to influence endosome localization and motility (Rocha et al., 2009; Jongsma et al., 2016; Raiborg et al., 2015a) and control core processes pertaining to endosome physiology, including cargo sorting (Dong et al., 2016; Eden et al., 2010, 2016) and membrane tethering, fusion, and fission events (Rowland et al., 2014; Wijdeven et al., 2016; Hoyer et al., 2018; van der Kant et al., 2013; Levin-Konigsberg et al., 2019). The rapidly growing diversity in ER-endosome contacts underscores both the importance and complexity of the dialog occurring between these organelles.

It is becoming increasingly clear that specific functional states of endocytic organelles are connected to their intracellular location (Jia and Bonifacino, 2019; Johnson et al., 2016;
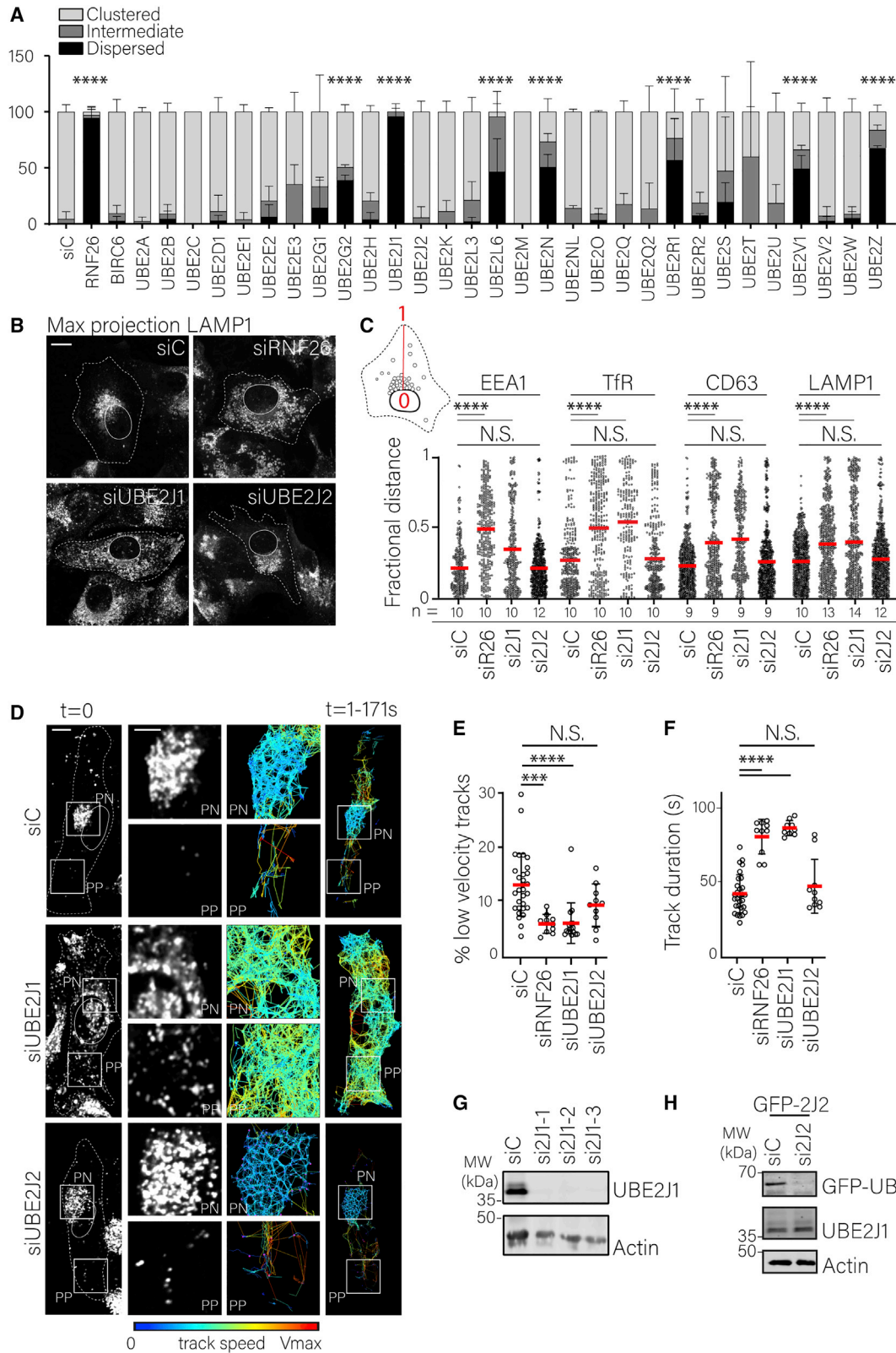
(legend on next page)

Korolchuk et al., 2011), an attribute that is strongly influenced by ER-endosome interactions (Neefjes et al., 2017). Under normal circumstances, the bulk of endosomes and lysosomes congregates in a perinuclear (PN) cloud around the microtubule-organizing center (MTOC). While many endosomes and lysosomes participating in this cloud tend to exhibit limited motility (Jongsma et al., 2016), some become subject to fast transport to and from the cell periphery (Bonifacino and Neefjes, 2017). This bilateral organization between the PN and peripheral (PP) regions of the cell appears critical for efficient maturation of endosomes and, consequently, timely degradation of cargos, such as the epidermal growth factor receptor (EGFR) (Jongsma et al., 2016). PN retention of endolysosomes is governed by the ER-located ubiquitin ligase RNF26, an integral multimembrane-spanning protein featuring a cytoplasmically exposed RING domain (Jongsma et al., 2016; Qin et al., 2014; Fenech et al., 2020). RNF26 is concentrated predominantly in the PN segment of the ER membrane, which corresponds with its ability to position all endosomal vesicles in the PN region of the cell (Jongsma et al., 2016). Catalytically competent RNF26 attracts and ubiquitylates SQSTM1/p62, a cytosolic ubiquitin adaptor also implicated in selective autophagy (Lamark et al., 2017), and the resulting ubiquitin-rich complex then recruits various endosomal adaptors capable of ubiquitin recognition to dock at the ER (Jongsma et al., 2016). How ubiquitin ligase activity of RNF26 is regulated to fulfill this role is unknown.

Ubiquitylation, orchestrated by a hierarchical enzymatic cascade (Pickart, 2001), is pervasive in endosome biology (Polo, 2012; Raiborg and Stenmark, 2009; McCann et al., 2016). To become biologically useful, ubiquitin must first be activated by an E1 enzyme. Next, an E2 enzyme receives this activated ubiquitin and can either pass it on to an independent E3 enzyme (as in the case of the HECT family of E3 ligases) or join forces with a RING-type E3 to directly mediate the transfer of ubiquitin to a substrate of choice (Stewart et al., 2016). While in mammals only 2 E1 enzymes for ubiquitin are known, roughly 40 E2 conjugating enzymes and >600 E3 ligases have been identified (Zheng and Shabek, 2017). This implies that E2 enzymes

usually support multiple E3 ligases, and a given E2 is likely to be involved in diverse biological processes (Gundogdu and Walden, 2019; Kwon and Ciechanover, 2017). A key missing piece in understanding ubiquitin-regulated positioning of vesicles by the RNF26-associated complex is the contribution of a cognate E2 enzyme. Here, we identify UBE2J1 as the conjugating enzyme collaborating with RNF26 in the regulation of the PN endosome cloud and show that through ubiquitylation of SQSTM1, and consequent vesicle adaptor recruitment onto the positioning complex, UBE2J1 promotes the integrity of the endolysosomal cloud. Consequently, UBE2J1 activity, like that of RNF26, facilitates ligand-mediated trafficking of EGFR to the late compartments and ensures timely inactivation of the downstream AKT signaling cascade. Since UBE2J1 is an E2 that is extensively implicated in ER-associated protein degradation (ERAD) (Hagiwara et al., 2016; Lenk et al., 2002; Burr et al., 2011), these findings open doors to possible interplay between ERAD and the PN endolysosomal cloud.

RESULTS

Depletion of UBE2J1 scatters the PN cloud

Given that the E3 ligase RNF26 uses ubiquitylation to position endosomes and lysosomes, there must also be a collaborating E2 enzyme. To identify E2 ubiquitin conjugating enzymes participating in the formation and maintenance of the PN endosomal cloud, we performed a depletion-based microscopy screen for known ubiquitin E2 enzymes in the human melanoma MelJuSo cell line, which was scored on the intracellular distribution of late endosomes (Figures 1A and S1A). Small interfering RNA (siRNA)-mediated silencing of several ubiquitin E2s (UBE2G2, UBE2J1, UBE2L6, UBE2N/UBE2V1, UBE2R1, and UBE2Z) was found to perturb the PN accumulation of endolysosomes marked by the human leukocyte antigen (HLA-DR) (Figures 1A and S1B). Among these potential E2 hits, silencing of UBE2J1 afforded the most striking relocalization of the HLA-DR$^+$ compartment (Figure 1A), and we therefore focused subsequent validation on UBE2J1 as a candidate E2 for RNF26.

Figure 1. UBE2J1 is required for the integrity of the endolysosomal cloud

(A) An siRNA-based screen for ubiquitin conjugating enzymes involved in the maintenance of the perinuclear (PN) endolysosomal cloud. MelJuSo cells depleted as indicated were immunostained against the late endosomal cargo HLA-DR (see also Figure S1) and scored on their vesicle distribution: clustered (white), intermediate (light gray), or dispersed (dark gray); n = 3–5 images (5–15 cells per image) analyzed per condition from 3 independent experiments.

(B) Distribution of endolysosomes in response to depletion of UBE2J1 or UBE2J2 relative to that of RNF26. Representative confocal z projections of fixed MelJuSo cells transfected with the indicated siRNAs and immunostained against LAMP1 (white) are shown.

(C) Intracellular distribution of early (EEA1), recycling (TfR), and late endosomes (CD63) and lysosomes (LAMP1) expressed as fractional distance of fluorescent pixels along a straight line drawn through the endolysosomal cloud from the nuclear edge (0) to the plasma membrane (1.0), as analyzed from samples in (A) and Figure S2A; n: number of cells analyzed per condition from 2 independent experiments.

(D) Organization and dynamics of late compartments as a function of UBE2J1 or UBE2J2 depletion. Left panels: representative confocal images of live MelJuSo cells transfected as indicated and treated with LysoTracker FarRed taken at the start of time-lapse, t = 0. Right panels: vesicle displacement rates depicted on a rainbow color scale (blue: immobile; red: maximum mobility per time interval) tracked over 171 s at 1.62 s per frame using the TrackMate plugin for Fiji. Boxed magnifications highlight select PN and peripheral (PP) regions. See also Videos S1, S2, and S3.

(E and F) Quantification of vesicle motility in control MelJuSo cells (siC) versus those depleted of either RNF26, UBE2J1, or UBE2J2. Bar graphs report the mean percentage of low-velocity tracks (as defined in Figure S1D) per cell (E) or total track duration (F), n_{siC} = 20, $n_{siRNF26}$ = 10, $n_{siUBE2J1}$ = 10, and $n_{siUBE2J2}$ = 10 cells analyzed per condition from n = 2 independent experiments.

(G and H) Western blot analyses of knockdown efficiencies for (G) UBE2J1 and (H) overexpressed GFP-UBE2J2.

Cell and nuclear boundaries are demarcated using dashed and continuous lines, respectively. Scale bars: 10 μm. Boxed images scale bars: 5 μm. Graphs report the mean (red line) of sample values (open circles), and error bars reflect ± SD. All significance was assessed with Student's t test, ***p < 0.001; ****p < 0.0001.
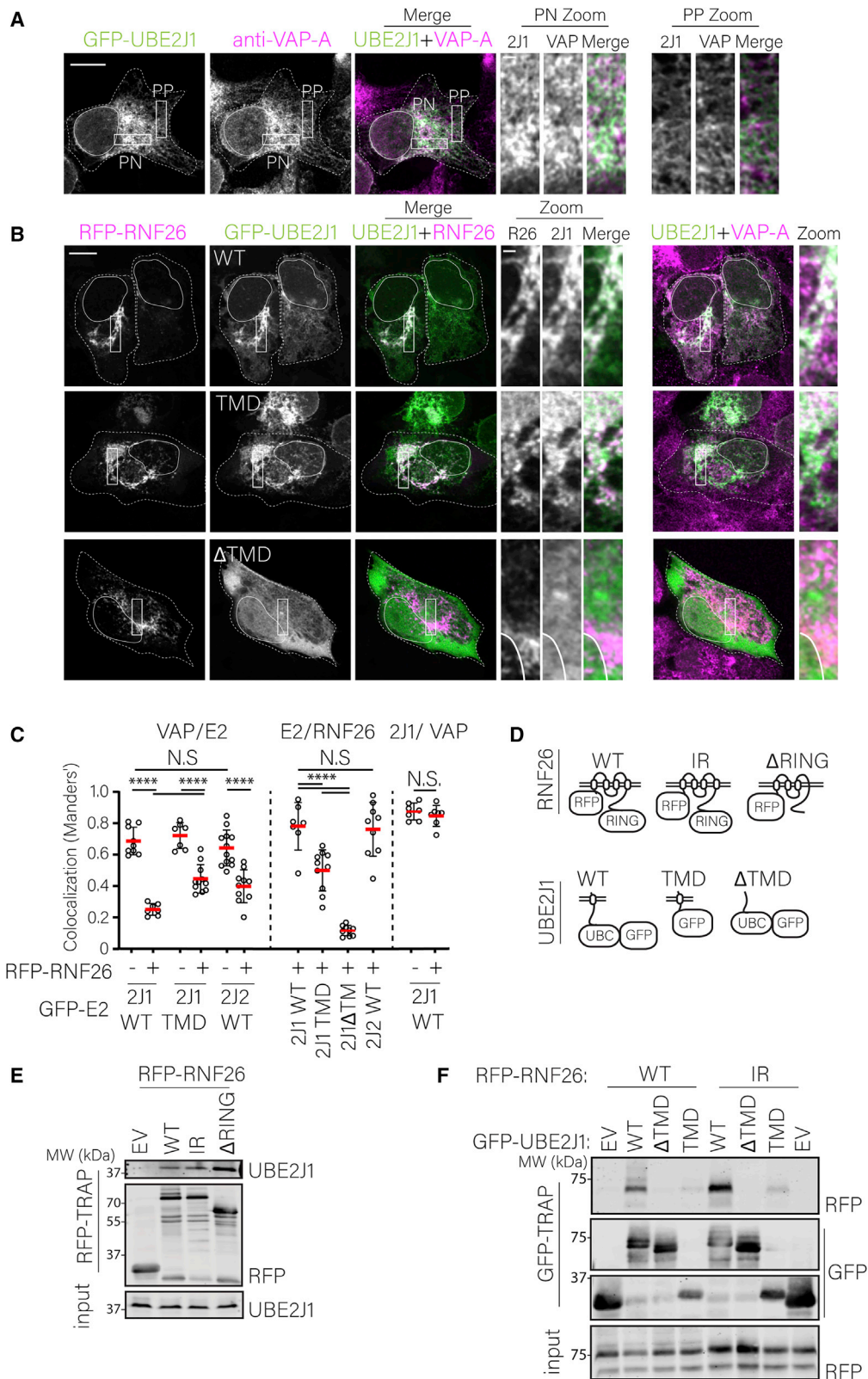
(legend on next page)

We have previously shown that the PN cloud harbors the entire endolysosomal pathway, including early, late, and recycling sub-compartments, and that the loss of RNF26 affects them all (Jongsma et al., 2016). The depletion of UBE2J1 phenocopied that of RNF26, resulting in the scattering of early (EEA1$^+$) and recycling (TfR$^+$) endosomes, as well as late endosomes (CD63$^+$) and lysosomes (LAMP1$^+$) throughout the cytoplasm (Figures 1B, 1C, and S2A–S2C). By contrast, depletion of its closest homolog, UBE2J2, did not alter endosomal positioning in cells (Figures 1A–1C and S2A). Next, considering that breakdown of the PN cloud leads to disordered vesicle transport throughout the cell (Jongsma et al., 2016; Sapmaz et al., 2019), we tested whether UBE2J1 influences not only the position but also the movement of endolysosomes. Under control conditions, acidified compartments (marked by Lysotracker) display bimodal motility, with the majority of PN endolysosomes exhibiting restricted movement relative to a smaller pool of far more dynamic PP vesicles (Figure 1D; Video S1). This spatiotemporal distinction was abrogated by the depletion of UBE2J1, releasing vesicles normally retained in the PN cloud for fast transport throughout the cytoplasmic space (Figure 1D; Video S2). As a result, an overall increase in vesicle movement was observed upon the loss of UBE2J1, resembling the condition of RNF26 deficiency (Figures 1E, 1F, and S2D). Once again, silencing UBE2J2 did not phenocopy the loss of RNF26 (Figures 1D–1F; Video S3), implying specificity on the part of UBE2J1 in the spatiotemporal regulation of the endolysosomal system.

Transmembrane interactions underpin UBE2J1/RNF26 complex in the juxtanuclear ER subdomain

For UBE2J1 to act as an E2 enzyme for RNF26, the two proteins must come in contact at the ER membrane. RNF26 is a multipass transmembrane protein (Qin et al., 2014) located in a PN subdomain of the ER (Jongsma et al., 2016). Strikingly, co-expression of RNF26 focused UBE2J1 into the PN ER region, as evidenced by the high degree of colocalization between RNF26 and UBE2J1 accompanied by a marked decrease in the fraction of VAP-A (general ER marker) positive for UBE2J1 (Figures 2A–2C). Conversely, the silencing of RNF26 resulted in a more uniform distribution of endogenous UBE2J1 throughout the ER (Figure S3A), while the knock out of UBE2J1 did not alter localization of RNF26 to the PN ER (Figures S3B and S3C). In addition, the examination of UBE2J1 distribution in live cells expressing a fluorescent ER marker (GFP fused to the transmembrane segment of MOSPD2; Di Mattia et al., 2018) in the presence of exogenous RNF26 (Figure S3D) lent further support to the aforementioned relocalization of UBE2J1 within the ER membrane. Shifting the cells to hypotonic conditions to induce fragmentation of the ER into large intracellular vesicles (King et al., 2020) revealed that, in response to RNF26 overexpression, UBE2J1 occupies discrete ER membrane subdomains (Figure S3D), resembling phase separation of proteins at ER MCSs (King et al., 2020).

Next, to characterize the requirements for UBE2J1/RNF26 complex formation, we designed mutant forms of both proteins (Figure 2D) and examined their contribution to the colocalization and interaction between UBE2J1 and RNF26. We found that the transmembrane domain (TMD) of UBE2J1, which on its own takes up residence throughout the ER membrane (Figure S4A), could be drawn into the PN region by RNF26, albeit to a lesser degree than the full-length UBE2J1 (Figures 2B and 2C). However, UBE2J1 lacking its TMD did not colocalize with RNF26, but remained dispersed throughout the cytosol (Figures 2B and 2C), implying that the ER-embedded TMD of UBE2J1 is necessary for complex formation with RNF26. In line with these observations, RNF26 co-isolated with both endogenous and ectopically expressed full-length UBE2J1 (Figures 2E and 2F), but not with its TMD-deficient soluble fragment (Figure 2F). In the same setting, the TMD-containing fragment alone afforded only a slight recovery of RNF26, implying that productive complex formation between UBE2J1 and RNF26 likely benefits from additional determinants. Besides UBE2J1, RNF26 was also found to interact and colocalize with UBE2J2 (Figures S4B–S4D), the loss of which did not influence the intracellular localization or behavior of the endolysosomal system (Figure 1). We therefore examined whether UBE2J1, but perhaps not UBE2J2, shares the substrate SQSTM1 of RNF26, as described below.

UBE2J1 mediates ubiquitylation of SQSTM1

To bridge the ER and endosomes, RNF26 binds and ubiquitinates SQSTM1, which then functions as a ubiquitin-rich scaffold for endosomal adapters. To identify lysine residues that are ubiquitinatd by RNF26, we analyzed hemagglutinin (HA)-SQSTM1 immunoprecipitates by mass spectrometry (Figures 3A–3D). Under 76% sequence coverage, we identified lysine 435 (K435) as the predominant site of ubiquitin modification

Figure 2. RNF26 recruits UBE2J1 to a PN ER subdomain
(A–C) Effect of RNF26 on the distribution of UBE2J1 in the ER.
(A and B) Representative confocal images of fixed MelJuSo cells ectopically expressing full-length GFP-UBE2J1, its transmembrane domain (TMD), or a mutant lacking the TMD (ΔTMD) in the (A) absence or (B) presence of exogenous full-length RFP-RNF26, immunostained against VAP-A (general ER marker) are shown. Magnifications highlight select PN and PP regions. Cell and nuclear boundaries are demarcated using dashed and continuous lines, respectively; scale bars: 10 μm, boxed images scale bars: 1 μm.
(C) Colocalization (Manders' overlap) of GFP-UBE2J1, GFP-TMD, or GFP-UBE2J2 with RNF26, as sampled from (A), (B), and Figure S4. Fraction VAP-A overlap reports on perinuclearity of UBE2J1 or its mutants in the presence (+) or absence (−) of RNF26. $n_{EV/J1} = 9$, $n_{R26/J1} = 7$, $n_{EV/2J1TMD} = 7$, $n_{R26/2J1TMD} = 7$, $n_{EV/2J2} = 12$, and $n_{R26/2J2} = 10$ cells analyzed per condition from n = 2 independent experiments.
(D) Schematic representation of the UBE2J1 and RNF26 (mutant) constructs used.
(E and F) Analysis of the interaction between ectopically expressed RFP-RNF26 or its inactive mutants I382R (IR) and/or ΔRING with (E) endogenous UBE2J1 or (F) exogenous GFP-UBE2J1 and its truncation mutants TMD and ΔTMD by co-immunoprecipitation (coIP).
Graphs report the mean (red line) of sample values (open circles), and error bars reflect ± SD. All significance was assessed with Student's t test, ****p < 0.0001, N.S., not significant.
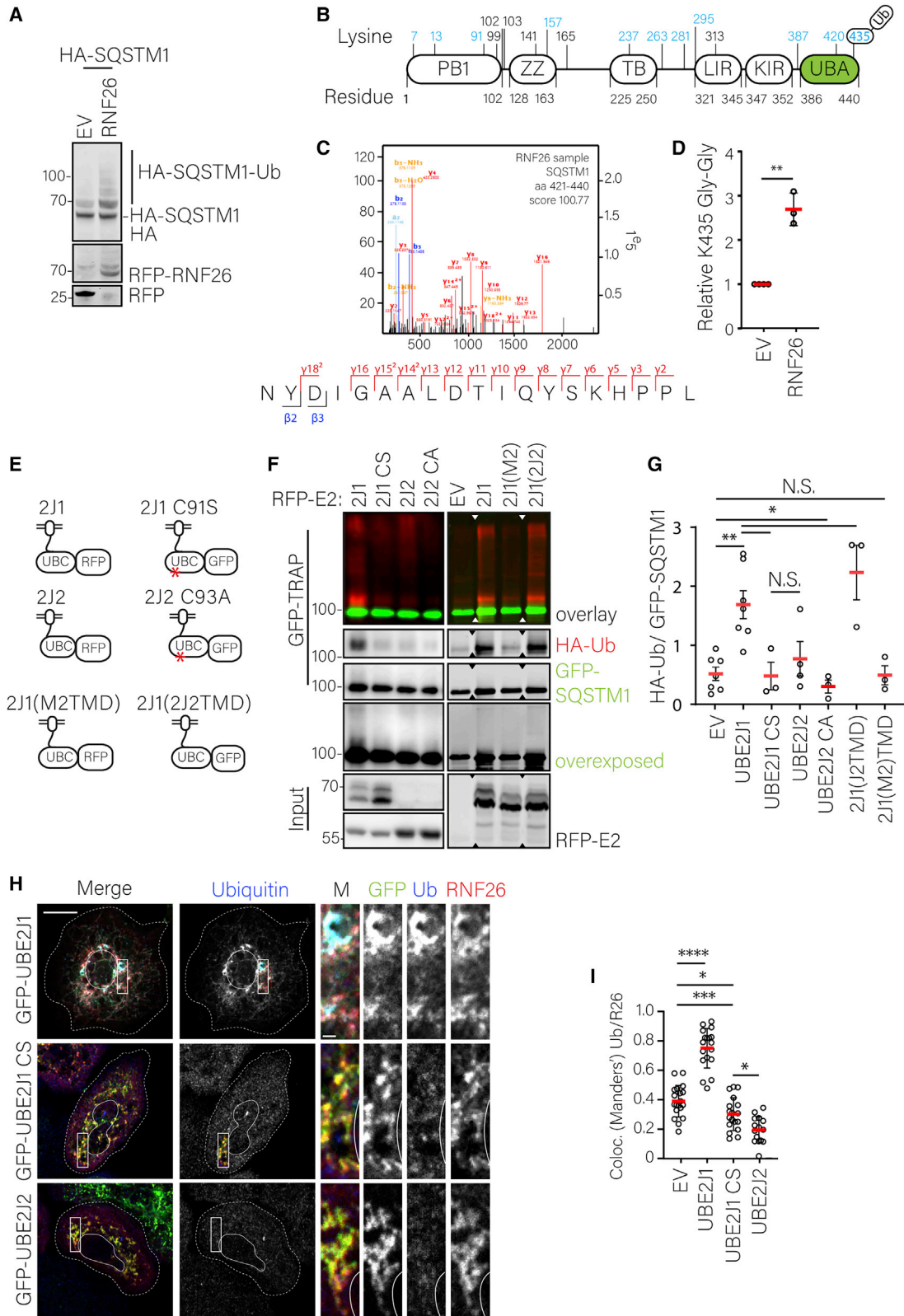
(legend on next page)

on SQSTM1, under both control conditions and in the presence of exogenous RNF26, as indicated by the double glycine motifs detected following trypsin digestion (Figures 3C, 3D, and S5A–S5C). In the latter case, substantially more peptides carrying modified K435 were observed (Figure 3D), consistent with the previously reported requirement for the UBA domain of SQSTM1 to propagate RNF26-dependent ubiquitylation signals (Jongsma et al., 2016). Next, we tested whether UBE2J1 also ubiquitylates SQSTM1. Ubiquitylation of SQSTM1 was markedly enhanced by the overexpression of catalytically competent UBE2J1, but not its inactive mutant C91S (Figures 3E–3G). In the same setting, UBE2J2 did not exhibit an effect on SQSTM1 ubiquitylation status (Figures 3E–3G), indicating that even though UBE2J2 can interact with RNF26 (Figure S4D), the two do not share SQSTM1 as a substrate. Interestingly, fusing the catalytic domain of UBE2J1 to the TMD of UBE2J2 (2J1(J2TMD)) still produced an ER-located enzyme capable of modifying SQSTM1 (Figures 3E–3G and S5D), while a similar chimera harboring the TMD of MOSPD2 (2J1(MSD2TMD)), an unrelated single-spanning protein anchored in the ER membrane, did not (Figures 3E–3G and S5D). We then tested whether RNF26 and UBE2J1 form a functionally competent complex inside the cell. As expected, the combination of RNF26 and catalytically active UBE2J1 stimulated the deposition of ubiquitylated species onto the E2/E3 complex. On the contrary, co-expression of either inactive UBE2J1 or wild-type (WT) UBE2J2 nearly abolished ubiquitylation at RNF26^{+} sites (Figures 3H and 3I). These results indicate that appropriate catalytic and TMD determinants are required on the part of the E2 to make a productive pair with RNF26 and suggest that a high degree of E2 selectivity operates in the pathways responsible for SQSTM1 ubiquitylation.

UBE2J1 participates in recruitment of vesicle adaptors to RNF26

To investigate whether UBE2J1 catalytic activity is required for PN endosome positioning, we performed rescue experiments in the background of UBE2J1 ablation. Similar to the siRNA-mediated depletion phenotype in MelJuSo cells (Figure 1), UBE2J1 knockout (KO) in HeLa cells featured a dispersed late endosomal compartment (Figures 4A–4C), despite the fact that ectopically expressed RNF26 was still localized in the PN ER (Figure S3B and S3C). Re-expression of WT UBE2J1 in this setting, but not that of its catalytically dead mutant, facilitated the centering of late endosomes in the PN area (Figures 4A–4C). This implies that a functional UBE2J1 enzyme is required for the maintenance of the PN cloud. We then set out to examine whether this E2 enzyme plays an active role in the recruitment of vesicle adaptor proteins to the RNF26-positioning complex. As a consequence of RNF26 enzymatic action, SQSTM1 is ubiquitylated for recognition by a number of endosomal membrane adaptors that contain a ubiquitin-binding domain. These adaptors include EPS15 and TOLLIP, which link early and late endosomes, respectively, to the ER-embedded positioning complex (Jongsma et al., 2016). Applying the hypotonic shock technique in this setting revealed RNF26 accumulation at sites of membrane opposition between the ER and endosome-associated TOLLIP (Figure 4D; Video S4). We hypothesized that perturbation in the cognate E2 activity would then inhibit ubiquitin-dependent bridges between the ER and endosomes. Ectopic expression of inactive but not WT UBE2J1 strongly diminished the colocalization of TOLLIP and EPS15 with RNF26 (Figures 4E, 4F, and S6A), supporting a pivotal role of the ubiquitin conjugating activity of UBE2J1 in endosome positioning.

Figure 3. UBE2J1 activity is required for RNF26 function

(A–D) Identification of the ubiquitylation site on SQSTM1 targeted by RNF26.

(A) Immunoblot analysis of HA-SQSTM1 precipitates from HEK293 cells cotransfected with either empty vector (EV) or RFP-RNF26 subsequently prepared for mass spectrometric analysis.

(B) Schematic overview of SQSTM1 protein sequence and domain organization (N to C terminus); Phox and Bem1p (PB1), zinc finger (ZZ), TRAF6-binding (TB), LC3-interacting (LIR), Keap-interacting (KIR), and ubiquitin-associated (UBA) domains. Lysines (K) present (blue) and absent (black) in SQSTM1 peptides identified by mass spectrometry following tryptic digestion are indicated.

(C) Representative ion spectrum of a Gly-Gly-modified SQSTM1 peptide spanning amino acid stretch 421–440, identifying ubiquitylation of K435 with its accompanying MaxQuant score.

(D) Quantification of Gly-Gly motifs on K435 of SQSTM1 normalized to the total number of SQSTM1 peptides harboring K435 expressed relative to EV, n = 3 independent experiments.

(E–G) Effect of UBE2J1 catalytic activity on SQSTM1 ubiquitylation status.

(E) Scheme of UBE2J1, UBE2J2, and E2 UBC mutants (asterisks) and TMD swap mutants used.

(F) Analysis of GFP-SQSTM1 ubiquitylation as a function of UBE2J1 or UBE2J2 overexpression. GFP-SQSTM1 (green) was immunoprecipitated from cells co-expressing HA-ubiquitin (red) and either RFP-UBE2J1 versus mutants C91S, MSD2TMD, and 2J2TMD or RFP-UBE2J2 versus mutant C93A or vector control (EV) under denaturing conditions. Western blot analyses of precipitates and the corresponding total cell lysates (Input) are shown. Triangles indicate where lanes were excised from the original scan.

(G) Quantification of ubiquitylated GFP-SQSTM1 relative to total GFP-SQSTM1 abundance; n_{EV} = 7, n_{2J1} = 7, n_{2J1CS} = 3, n_{2J2} = 4, n_{2J2CS} = 12, $n_{2J1(2J2TMD)}$ = 3, and $n_{2J1(M2TMD)}$ = 3 independent experiments.

(H and I) Ubiquitin recruitment to RNF26/UBE2J1[+] structures as a function of UBE2J1 activity.

(H) Representative confocal images of HeLa cells expressing HA-RNF26 and either GFP-UBE2J1 or C91S (green). Cells were immunostained for HA (red) and ubiquitin (blue). Representative confocal fluorescence overlays (merge) and magnifications along with black-white single-channel images are shown. Cell and nuclear boundaries are demarcated using dashed and continuous lines, respectively. Scale bars: 10 μm, magnified images scale bar: 1 μm.

(I) Colocalization (Manders' overlap) between ubiquitin and HA-RNF26 as a function of UBE2J1/J2; n_{EV} = 19, n_{2J1} = 18, n_{2J1CS} = 18, and n_{2J2} = 15 cells analyzed from 3 independent experiments.

Scale bars: 10 μm. Magnified images scale bar: 1 μm. Graphs report the mean (red line) of sample values (open circles), and error bars reflect ± SD. All significance was assessed with Student's t test, *p < 0.05; **p < 0.01; ***p < 0.001; ****p < 0.0001, N.S., not significant.
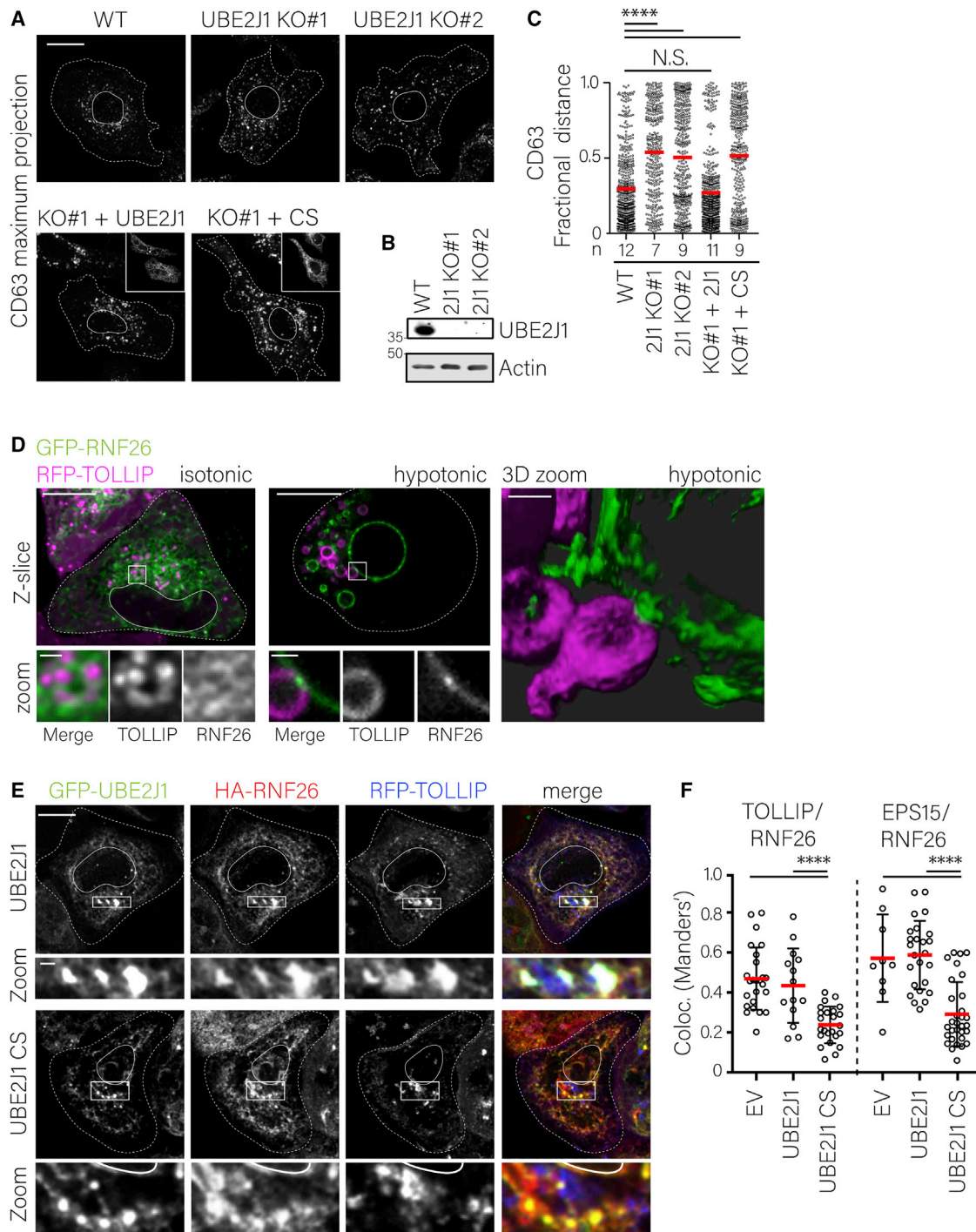
Figure 4. UBE2J1 catalytic activity is required for vesicle recruitment to RNF26

(A) WB validation of UBE2J1 KO in 2 clonal cell lines created by CRISPR-Cas9 vector transfection and limiting dilution. Actin was used as a loading control. The position protein marker is indicated.

(B) Late endosome distribution in WT HeLa cells, 2 UBE2J1 KO clones, or KO#1 cells that express either GFP-UBE2J1 WT or inactive GFP-CS. Representative maximum projection confocal images of CD63 immunostaining is shown. Insets show GFP-UBE2J1 expression in rescue cells.

(C) Vesicle localization depicted as fractional distance, as in Figure 1C of samples in (A). Results from 2 independent experiments; significance was tested versus HeLa WT sample. n: number of cells analyzed per condition.

(D) Visualization of contacts between GFP-RNF26 and RFP-TOLLIP structures. Live cell HeLa cells were imaged under isotonic or hypotonic conditions. Shown are overlays and zooms of TOLLIP[+] structures that closely interact with RNF26^{+} membranes under isotonic conditions and TOLLIP[+] large intracellular vesicles

(legend continued on next page)

UBE2J1 promotes timely downregulation of EGFR

Spatiotemporal organization of the endosomal system translates into efficient trafficking of cargoes to the proteolytic compartment (Jongsma et al., 2016). If acting upstream of RNF26, then UBE2J1 is also expected to facilitate this process. To test this, we followed ligand-mediated trafficking and degradation of EGFR. In control cells, EGF$^+$ vesicles were quickly targeted to the PN cloud, but in cells compromised for UBE2J1, the EGF$^+$ compartment remained disorganized (Figures 5A and 5B). While the entry of activated EGFR into EEA1$^+$ early endosomes was not affected by the silencing of UBE2J1 (Figures 5A and 5C), its maturation into the CD63$^+$ late compartments was strongly inhibited (Figures 5A, 5C, and S6B). Consequently, these cells exhibited attenuated downregulation of stimulated EGFR and a marked prolongation of the activated receptor state (Figures 5D and 5E). Given that UBE2J1 silencing did not alter steady-state levels of EGFR at the cell surface (Figure 5F), the above results indicate that UBE2J1 promotes timely trafficking and downregulation of EGFR in response to ligand treatment. They further suggest that in cells deficient for UBE2J1, downstream signaling should be prolonged. EGFR activation is known to engage multiple downstream pathways, including signaling along the PI(3)K-AKT axis (Sugiyama et al., 2019). We found that silencing of either UBE2J1 or RNF26 enhanced and prolonged EGF-induced phosphorylation of AKT, particularly on serine 473 (S473) (Figures 6A and 6B), which is mediated by mammalian target of rapamycin complex 2 (mTORC2) on endosomal membranes and required for the full activation of AKT (Sugiyama et al., 2019). Taken together with delays in EGFR trafficking, these results underscore the physiological role of UBE2J1 in the regulation of the architecture and dynamics of the endosomal system, with implications for membrane-dependent signaling pathways (Figure 6C).

DISCUSSION

Endosomes rely on the ER to facilitate the timely processing and selective delivery of cargoes for degradation. One aspect in which this manifests is the architectural support that the ER offers to the PN endosome cloud—the cell's hub for endosomal maturation and proteolysis (Neefjes et al., 2017). In this study, we implicate the ER-associated ubiquitin conjugating enzyme UBE2J1 in the PN positioning of the endolysosomal system. The depletion of UBE2J1 disturbs the PN vesicle cloud, where the bulk of these structures is normally retained in a low motility state. This leads to deregulated motility patterns of endosomes

and lysosomes throughout the cell and delays ligand-mediated trafficking of activated receptors to the proteolytic compartments. Consequently, phosphorylated receptor half-life is increased, resulting in the prolongation of downstream signaling events, particularly through the phosphorylation of AKT on S473, which may be due to the misregulation of membrane-associated site-specific AKT kinases and phosphatases (Sugiyama et al., 2019). Because dephosphorylation of EGFR itself is known to occur at MCSs between receptor-containing endosomes and the ER (Eden et al., 2010, 2016), persistence of the activated receptor state in cells compromised for UBE2J1 suggests a potential for collaboration between the mechanisms of endosome positioning and phosphatase engagement, both facilitated by the ER.

We find that the catalytic activity of UBE2J1 is a prerequisite for the maintenance of PN architecture of the endolysosomal system, achieved in part through the recruitment of specialized endosomal adaptors to the ubiquitin-dependent positioning complex assembled by its partner RING E3 ligase RNF26 at the ER membrane (Jongsma et al., 2016). We propose that UBE2J1 serves as an E2 for RNF26, and that endosomal phenotypes associated with UBE2J1 loss-of-function arise due to the inactivity of this PN positioning pathway. UBE2J1 has been extensively studied in the context of ERAD and stress recovery (Burr et al., 2011; Elangovan et al., 2017; Hagiwara et al., 2016; Lenk et al., 2002; Tiwari and Weissman, 2001), and its physiological roles in viral infection (Ma et al., 2015; Feng et al., 2018) and spermiogenesis (Koenig et al., 2014) are thought to be mediated through ERAD functions. Our data reveal an unexpected role for UBE2J1, which brings about the possibility that deleterious phenotypes associated with the dysfunction of this enzyme may also stem from defects in endosomal trafficking.

Several studies have shown that the nature of the TMD of UBE2J1 determines its activity and stability (Claessen et al., 2010; Yang et al., 1997). Likewise, our data suggest that the interaction of UBE2J1 with RNF26 is stabilized partly through their respective TMDs. Interestingly, E3 and E1 binding sites on the UBC domain of an E2 enzyme usually overlap (Stewart et al., 2016), resulting in mutually exclusive binding. Thus, extra TMD-mediated E2-E3 interactions may potentiate the ubiquitin cascade, since UBE2J1 may remain bound to RNF26 while accepting freshly activated, E1-derived ubiquitin for subsequent rounds of ubiquitylation. Conversely, the localization of this E2-E3 complex to a PN subdomain of the ER is specified by the RING domain of RNF26. The resulting ER-embedded

---

(ICLVs) that are situated directly next to RNF26$^+$ ICLVs under hypotonic conditions (crosshairs). White color in 3D representation represents the membrane contact site between 2 opposing membranes.

(E) TOLLIP recruitment to RNF26$^+$ structures as a function of UBE2J1 activity. Confocal microscopy images of HeLa cells overexpressing RFP-TOLLIP HA-RNF26 and WT or mutant (CS) GFP-UBE2J1. Shown are the separate channels and merged images of UBE2J1 (green), RNF26 (red), and TOLLIP (blue), and select magnifications.

(F) Quantification of overlap between HA-RNF26 and RFP-TOLLIP (4E) or GFP-EPS15 signal (see Figure S5B) in HeLa cells overexpressing either UBE2J1 WT or mutant UBE2J1 CS, or EV control from (E). $n_{Tollip/EV}$ = 24, $n_{Tollip/WT}$ = 13, $n_{Tollip/CS}$ = 24, $n_{EPS15/EV}$ = 9, and $n_{EPS15/WT}$ = 31 cells analyzed from 3 independent experiments.

Scale bars: 10 μm. Magnified images scale bar: 1 μm. Cell and nuclear boundaries are demarcated using dashed and continuous lines, respectively. Graphs report the mean (red line) of sample values (open circles), and error bars reflect ± SD. All significance was assessed with Student's t test, *p < 0.05; **p < 0.01; ***p < 0.001; ****p < 0.0001, N.S., not significant.
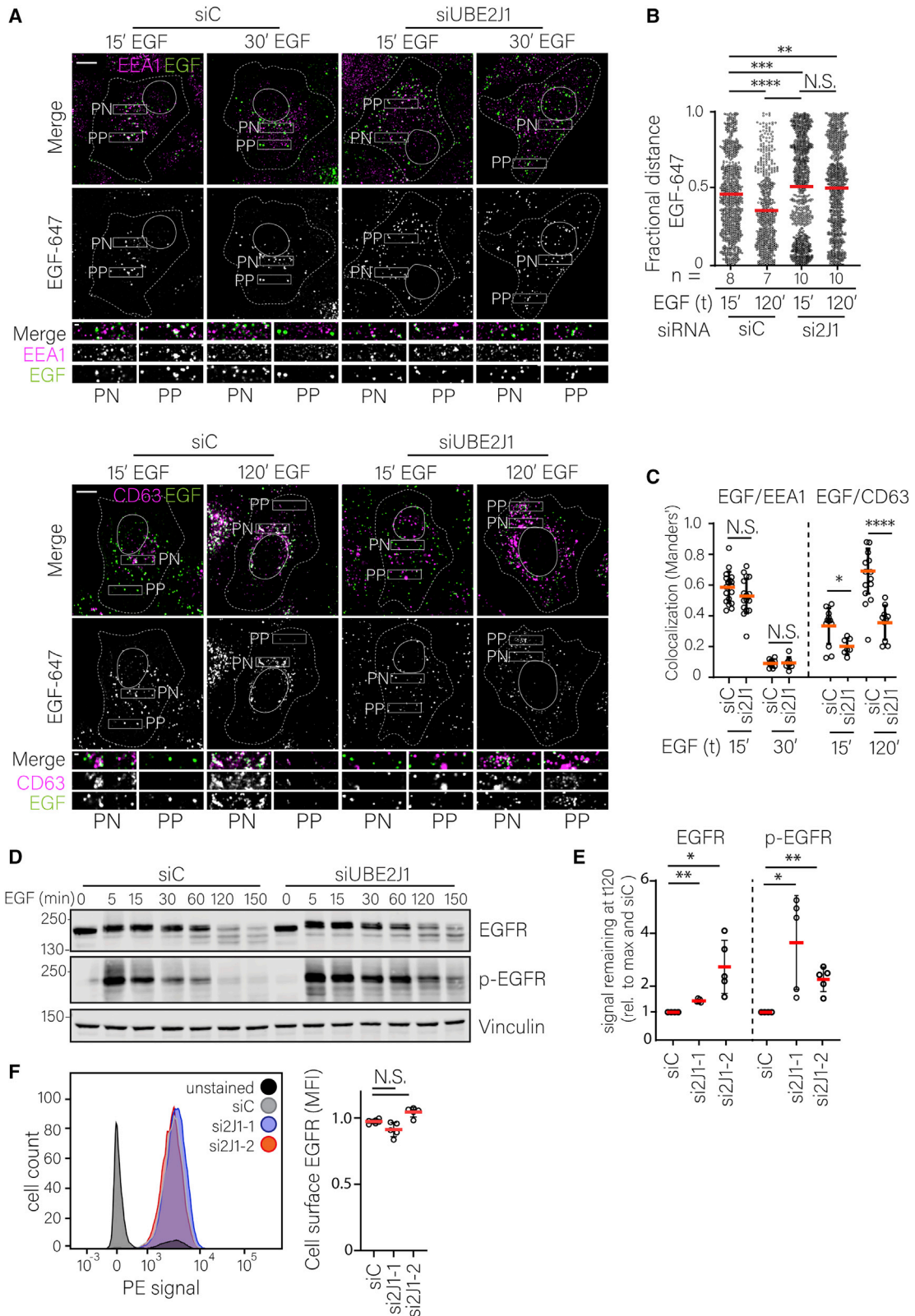
(legend on next page)

ubiquitylation complex modifies SQSTM1, thereby enticing ubiquitin-binding vesicle adaptors to dock at the ER membrane. Our results pinpoint that UBE2J1/RNF26-mediated ubiquitin conjugation on SQSTM1 targets K435, which is located on the C-terminal side of its ubiquitin-binding UBA domain. By contrast, the neighboring K420, reported to facilitate SQSTM1 function in autophagic cargo sequestration (Lee et al., 2017), remains unaffected by the activity of the ER-associated endosome positioning complex, suggesting that ubiquitylation on specific sites of SQSTM1 promotes selectivity toward different cellular functions of this versatile ubiquitin adaptor.

Thus, UBE2J1, an E2 enzyme primarily known for conducting ubiquitylation that targets substrates for proteasomal degradation (Feng et al., 2018), is now also implicated in ubiquitin modification in support of the spatiotemporal regulation of organelle behavior. Interestingly, we find that UBE2J2, also residing in the ER membrane as part of the ERAD machinery (Wang et al., 2009; Weber et al., 2016), can similarly associate with RNF26, but does not support ubiquitin transfer to SQSTM1. In fact, the overexpression of UBE2J2 appears to act as a dominant-negative for the UBE2J1/RNF26 pair. This pseudo-compatibility of UBE2J2 may relate to its cytoplasmic fragment, which is shorter than that of UBE2J1, perhaps making it more difficult for its UBC domain to reach substrates bound by the RING domain of RNF26. Despite sharing a common ancestor (Lenk et al., 2002), these sister E2 enzymes have evolved in different ways and mediate ubiquitin transfer for distinct cellular processes (van de Weijer et al., 2017; Burr et al., 2011; van de Weijer et al., 2014). For instance, both E2 enzymes can be degraded by the proteasome, although the degradation of UBE2J1 requires certain conditions that induce its phosphorylation, while UBE2J2 cannot be phosphorylated (Elangovan et al., 2017; Lam et al., 2014). Apparently, the more complex mammalian cellular environment required the need for a more diverse set of ER-associated ubiquitin conjugating enzymes. Single-spanning TMD proteins, such as the aforementioned E2s, may be required for the organization of large membrane-embedded protein complexes, as illustrated by interactions within the mitochondrial respiratory chain complex (Zickermann et al., 2010).

A similar organizational principle could hold for complexes at and/or within the ER membrane.

In recent years, numerous proteins have been identified to participate in the formation and regulation of ER-endosome contact sites, each regulating specific stages or transitions of endosomal trafficking. A maturing endosome can likely engage in multiple tethering interactions, and the composition and duration of its interactions with the ER could be influenced by maturation. Membrane proximity invoked by dynamic ubiquitin-mediated interactions, as described here, may enhance the strength and/or duration of ER-endosome membrane contact sites, providing a fundament for robust yet agile regulatory interactions. Finally, the UBE2J1/RNF26 endosomal positioning complex locates to defined PN compartments of the ER that may be co-occupied by members of the ERAD family (Leitman et al., 2014). The close proximity of ERAD to lysosomes could then allow for swift alternate degradation of ERAD-resistant substrates.

STAR★METHODS

Detailed methods are provided in the online version of this paper and include the following:

- KEY RESOURCES TABLE
- RESOURCE AVAILABILITY
  - Lead contact
  - Materials availability
  - Data and code availability
- EXPERIMENTAL MODEL AND SUBJECT DETAILS
  - Cell lines
- METHOD DETAILS
  - siRNA transfections
  - Constructs
  - DNA transfections
  - CRISPR/Cas9-mediated knockout
  - EGFR degradation
  - Immunofluorescence confocal microscopy
  - Live microscopy

Figure 5. UBE2J1 is required for timely degradation and inactivation of EGFR

(A–C) Trafficking of ligand-stimulated EGFR toward early endosomes or lysosomes in the presence or absence of UBE2J1.

(A) Representative confocal images show UBE2J1-1-depleted or control HeLa cells, stimulated with Alexa 647-labeled EGF (100 μg/mL) for 15 and 30 min (EEA1) or 15 and 120 min (CD63) before fixation and immunostaining against endosomal markers. Shown are single focal plane images of EGF (green) and endosomal markers (magenta) at the indicated time points, and magnifications of select PN and PP areas.

(B) Fractional distance analysis of EGF$^+$ structures at 15 or 120 min post-stimulation in si2J1-1 or control cells, as sampled from (A).

(C) Colocalization (Manders' overlap) of EGF-647 and EEA1 or CD63 in UBE2J1 silenced cells (si2J1-1) versus control cells at different time points post-EGF stimulation, sampled from (A). Quantification of $n_{EEA1/siC}$ = 18, $n_{EEA1/si2J1}$-15′ = 18, $n_{EEA1/siC30′}$ = 10, $n_{EEA1/si2J1-30′}$ = 8, $n_{CD63/siC}$ = 11, $n_{CD63/si2J1-15′}$ = 7, $n_{CD63/siC120′}$ = 14, $n_{CD63/si2J1-120′}$ = 10 cells from 2 independent experiments.

(D and E) Total and activated EGFR levels as a function of time in ligand-stimulated cells either depleted or not depleted with UBE2J1.

(D) Scans of western blots stained for total and activated (p-)EGFR, as well as vinculin (loading control) levels at indicated time points following EGF stimulation in siUBE2J1-1 or control cells.

(E) Quantification of total (EGFR, relative to t = 0) and activated (p-EGFR, relative to full activation at t = 5) receptor at 120 min after EGF stimulation, normalized to vinculin levels and to control. Shown are means ± SDs of 4 (si2J1-1) and 5 (si2J1-2) independent experiments.

(F) EGFR expression as determined by phycoerythrin (PE)-conjugated anti-EGFR flow cytometry (MFI) in cells transfected with UBE2J1 siRNA #1 or #2 or the control. Shown are means ± SDs of 5 independent experiments and representative plot of signal distribution.

See also Figure S6. Scale bar: 10 μm. Magnified images scale bar: 1 μm. Magnification identical for all images. Cell and nuclear boundaries are demarcated using dashed and continuous lines, respectively. Graphs report the mean (red line) of sample values (open circles), and error bars reflect ± SD. All significance was assessed with Student's t test, *p < 0.05; **p < 0.01; ***p < 0.001; ****p < 0.0001, N.S., not significant.
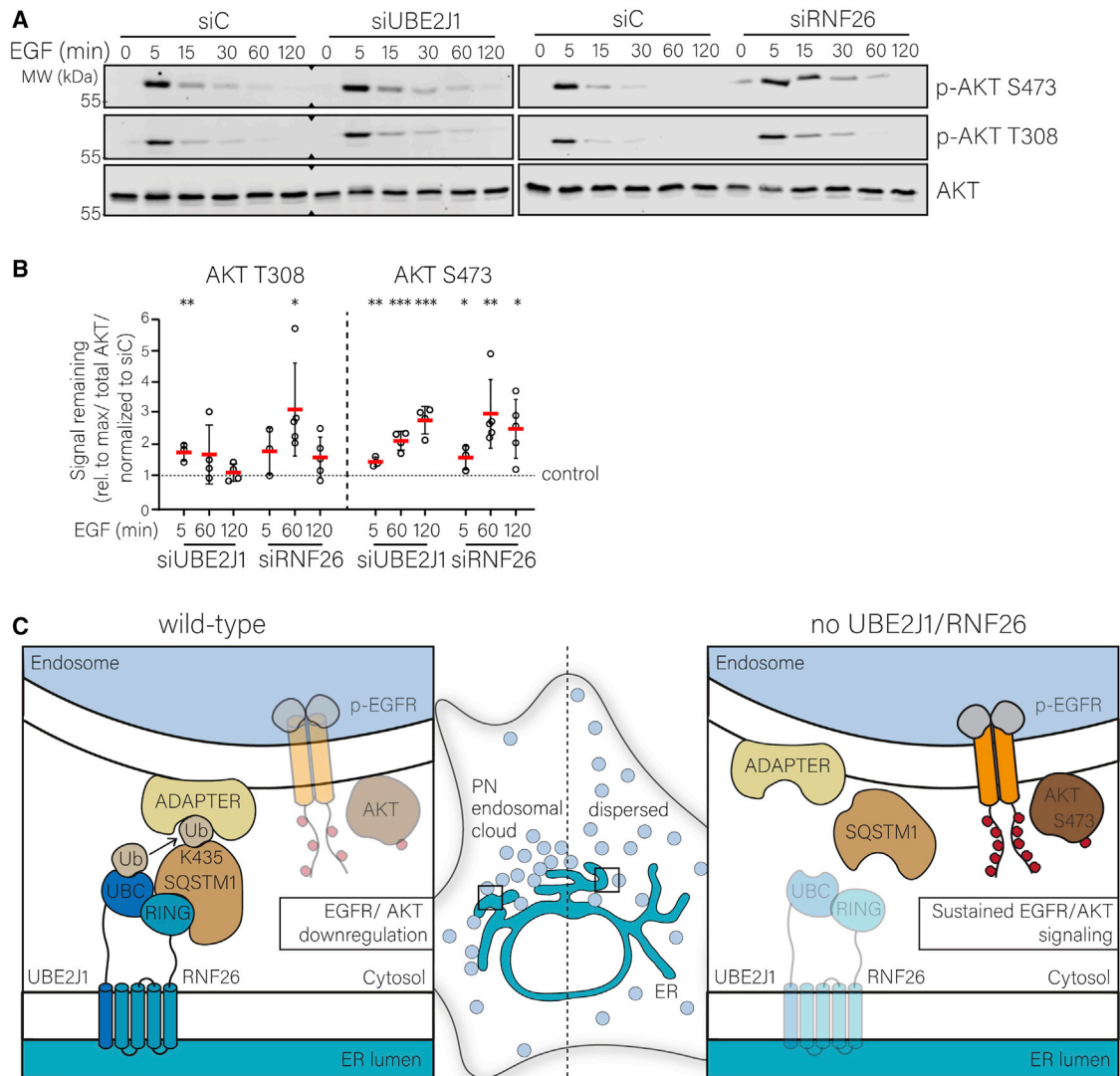
A

B

C

Figure 6. RNF26 and UBE2J1 are required for timely inhibition of EGF-induced AKT signaling

(A and B) Total and activated AKT levels as a function of time in ligand-stimulated cells either depleted or not depleted with siUBE2J1-1 or siRNF26.

(A) Scans of western blots stained for total and phosphorylated (threonine 308 or serine 473) AKT levels at indicated time points following EGF stimulation in UBE2J1-1 or RNF26-1 silenced or control cells.

(B) Quantification of relative amounts of EGF-induced AKT signaling, normalized to total AKT levels, full activation (t = 5), and to control (dashed line = 1). Four (UBE2J1) or 5 (RNF26) independent experiments. Significance tested with unpaired Student's t test.

(C) Model for regulation of PN endosomal organization by the RNF26/UBE2J1 complex, with consequences for EGF-induced receptor and AKT downregulation.

The TMDs of RNF26 bind the single TMD of UBE2J1 within the ER membrane to mediate the close proximity of the RNF26 RING domain to the ubiquitin-loaded UBE2J1 UBC domain that are both extending from the ER membrane into the cytosol, which further interact to govern ubiquitin transfer. The activated UBE2J1/RNF26 complex ubiquitinates SQSTM1 through mono-/short-chain linkage(s) modification of lysine residues, including K435, which in turn serves as a platform for the binding of vesicle adaptors such as EPS15 or TOLLIP via their ubiquitin-binding domains. Here, vesicles bound by vesicle adaptors are recruited to the PN endosomal cloud until release. As a result, EGFR and AKT signaling is downregulated in a timely manner. The loss of UBE2J1 or RNF26 results in endosomal dispersion, deconstruction of the RNF26 positioning complex, and deregulation of EGFR downregulation and membrane-associated AKT (S473) signaling.

- ○ Co-immunoprecipitations
- ○ Ubiquitylation assays
- ○ SDS-PAGE and western blotting
- ○ Flow cytometry

- ○ In-gel digestion
- ○ Mass spectrometry
- ○ MS data analysis
- ● QUANTIFICATION AND STATISTICAL ANALYSIS

Cell Reports
Article

REFERENCES

Bakker, J., Spits, M., Neefjes, J., and Berlin, I. (2017). The EGFR odyssey - from activation to destruction in space and time. J. Cell Sci. *130*, 4087–4096.

Berlin, I., Higginbotham, K.M., Dise, R.S., Sierra, M.I., and Nash, P.D. (2010). The deubiquitinating enzyme USP8 promotes trafficking and degradation of the chemokine receptor 4 at the sorting endosome. J. Biol. Chem. *285*, 37895–37908.

Bonifacino, J.S., and Neefjes, J. (2017). Moving and positioning the endolysosomal system. Curr. Opin. Cell Biol. *47*, 1–8.

Burr, M.L., Cano, F., Svobodova, S., Boyle, L.H., Boname, J.M., and Lehner, P.J. (2011). HRD1 and UBE2J1 target misfolded MHC class I heavy chains for endoplasmic reticulum-associated degradation. Proc. Natl. Acad. Sci. USA *108*, 2034–2039.

Cabukusta, B., Berlin, I., van Elsland, D.M., Forkink, I., Spits, M., de Jong, A.W.M., Akkermans, J.J.L.L., Wijdeven, R.H.M., Janssen, G.M.C., van Veelen, P.A., and Neefjes, J. (2020). Human VAPome Analysis Reveals MOSPD1 and MOSPD3 as Membrane Contact Site Proteins Interacting with FFAT-Related FFNT Motifs. Cell Rep. *33*, 108475.

Claessen, J.H., Mueller, B., Spooner, E., Pivorunas, V.L., and Ploegh, H.L. (2010). The transmembrane segment of a tail-anchored protein determines its degradative fate through dislocation from the endoplasmic reticulum. J. Biol. Chem. *285*, 20732–20739.

Cox, J., and Mann, M. (2008). MaxQuant enables high peptide identification rates, individualized p.p.b.-range mass accuracies and proteome-wide protein quantification. Nat. Biotechnol. *26*, 1367–1372.

Di Fiore, P.P., and von Zastrow, M. (2014). Endocytosis, signaling, and beyond. Cold Spring Harb. Perspect. Biol. *6*, a016865.

Di Mattia, T., Wilhelm, L.P., Ikhlef, S., Wendling, C., Spehner, D., Nominé, Y., Giordano, F., Mathelin, C., Drin, G., Tomasetto, C., and Alpy, F. (2018). Identification of MOSPD2, a novel scaffold for endoplasmic reticulum membrane contact sites. EMBO Rep. *19*, e45453.

Dong, R., Saheki, Y., Swarup, S., Lucast, L., Harper, J.W., and De Camilli, P. (2016). Endosome-ER Contacts Control Actin Nucleation and Retromer Function through VAP-Dependent Regulation of PI4P. Cell *166*, 408–423.

Eden, E.R., White, I.J., Tsapara, A., and Futter, C.E. (2010). Membrane contacts between endosomes and ER provide sites for PTP1B-epidermal growth factor receptor interaction. Nat. Cell Biol. *12*, 267–272.

Eden, E.R., Sanchez-Heras, E., Tsapara, A., Sobota, A., Levine, T.P., and Futter, C.E. (2016). Annexin A1 Tethers Membrane Contact Sites that Mediate ER to Endosome Cholesterol Transport. Dev. Cell *37*, 473–483.

Elangovan, M., Chong, H.K., Park, J.H., Yeo, E.J., and Yoo, Y.J. (2017). The role of ubiquitin-conjugating enzyme Ube2j1 phosphorylation and its degradation by proteasome during endoplasmic stress recovery. J. Cell Commun. Signal. *11*, 265–273.

Fenech, E.J., Lari, F., Charles, P.D., Fischer, R., Laétitia-Thézénas, M., Bagola, K., Paton, A.W., Paton, J.C., Gyrd-Hansen, M., Kessler, B.M., and Christianson, J.C. (2020). Interaction mapping of endoplasmic reticulum ubiquitin ligases identifies modulators of innate immune signalling. eLife *9*, 2020.03.18.993998.

Feng, T., Deng, L., Lu, X., Pan, W., Wu, Q., and Dai, J. (2018). Ubiquitin-conjugating enzyme UBE2J1 negatively modulates interferon pathway and promotes RNA virus infection. Virol. J. *15*, 132.

Gundogdu, M., and Walden, H. (2019). Structural basis of generic versus specific E2-RING E3 interactions in protein ubiquitination. Protein Sci. *28*, 1758–1770.

Hagiwara, M., Ling, J., Koenig, P.A., and Ploegh, H.L. (2016). Posttranscriptional Regulation of Glycoprotein Quality Control in the Endoplasmic Reticulum Is Controlled by the E2 Ub-Conjugating Enzyme UBC6e. Mol. Cell *63*, 753–767.

Hoyer, M.J., Chitwood, P.J., Ebmeier, C.C., Striepen, J.F., Qi, R.Z., Old, W.M., and Voeltz, G.K. (2018). A Novel Class of ER Membrane Proteins Regulates ER-Associated Endosome Fission. Cell *175*, 254–265.e14.

Huotari, J., and Helenius, A. (2011). Endosome maturation. EMBO J. *30*, 3481–3500.

Jewett, C.E., and Prekeris, R. (2018). Insane in the apical membrane: trafficking events mediating apicobasal epithelial polarity during tube morphogenesis. Traffic. https://doi.org/10.1111/tra.12579.

Jia, R., and Bonifacino, J.S. (2019). Lysosome Positioning Influences mTORC2 and AKT Signaling. Mol. Cell *75*, 26–38.e3.

Johnson, D.E., Ostrowski, P., Jaumouillé, V., and Grinstein, S. (2016). The position of lysosomes within the cell determines their luminal pH. J. Cell Biol. *212*, 677–692.

Jongsma, M.L., Berlin, I., Wijdeven, R.H., Janssen, L., Janssen, G.M., Garstka, M.A., Janssen, H., Mensink, M., van Veelen, P.A., Spaapen, R.M., and Neefjes, J. (2016). An ER-Associated Pathway Defines Endosomal Architecture for Controlled Cargo Transport. Cell *166*, 152–166.

Khaminets, A., Behl, C., and Dikic, I. (2016). Ubiquitin-Dependent And Independent Signals In Selective Autophagy. Trends Cell Biol. *26*, 6–16.

King, C., Sengupta, P., Seo, A.Y., and Lippincott-Schwartz, J. (2020). ER membranes exhibit phase behavior at sites of organelle contact. Proc. Natl. Acad. Sci. USA *117*, 7225–7235.

Koenig, P.A., Nicholls, P.K., Schmidt, F.I., Hagiwara, M., Maruyama, T., Frydman, G.H., Watson, N., Page, D.C., and Ploegh, H.L. (2014). The E2 ubiquitin-conjugating enzyme UBE2J1 is required for spermiogenesis in mice. J. Biol. Chem. *289*, 34490–34502.

Korolchuk, V.I., Saiki, S., Lichtenberg, M., Siddiqi, F.H., Roberts, E.A., Imarisio, S., Jahreiss, L., Sarkar, S., Futter, M., Menzies, F.M., et al. (2011). Lysosomal positioning coordinates cellular nutrient responses. Nat. Cell Biol. *13*, 453–460.

Kwon, Y.T., and Ciechanover, A. (2017). The Ubiquitin Code in the Ubiquitin-Proteasome System and Autophagy. Trends Biochem. Sci. *42*, 873–886.

Lam, S.Y., Murphy, C., Foley, L.A., Ross, S.A., Wang, T.C., and Fleming, J.V. (2014). The human ubiquitin conjugating enzyme UBE2J2 (Ubc6) is a substrate for proteasomal degradation. Biochem. Biophys. Res. Commun. *451*, 361–366.

Lamark, T., Svenning, S., and Johansen, T. (2017). Regulation of selective autophagy: the p62/SQSTM1 paradigm. Essays Biochem. *61*, 609–624.

Lee, Y., Chou, T.F., Pittman, S.K., Keith, A.L., Razani, B., and Weihl, C.C. (2017). Keap1/Cullin3 Modulates p62/SQSTM1 Activity via UBA Domain Ubiquitination. Cell Rep. *19*, 188–202.

Leitman, J., Shenkman, M., Gofman, Y., Shtern, N.O., Ben-Tal, N., Hendershot, L.M., and Lederkremer, G.Z.. (2014). Herp coordinates compartmentalization and recruitment of HRD1 and misfolded proteins for ERAD. Mol. Biol. Cell. *25*, 1050–1060.

Lenk, U., Yu, H., Walter, J., Gelman, M.S., Hartmann, E., Kopito, R.R., and Sommer, T. (2002). A role for mammalian Ubc6 homologues in ER-associated protein degradation. J. Cell Sci. *115*, 3007–3014.

Levin-Konigsberg, R., Montano-Rendon, F., Keren-Kaplan, T., Li, R., Ego, B., Mylvaganam, S., Diciccio, J.E., Trimble, W.S., Bassik, M.C., Bonifacino, J.S., Fairn, G.D., and Grinstein, S. (2019). Phagolysosome resolution requires contacts with the endoplasmic reticulum and phosphatidylinositol-4-phosphate signalling. Nat. Cell Biol. *21*, 1234–1247.

Ma, H., Dang, Y., Wu, Y., Jia, G., Anaya, E., Zhang, J., Abraham, S., Choi, J.G., Shi, G., Qi, L., et al. (2015). A CRISPR-Based Screen Identifies Genes Essential for West-Nile-Virus-Induced Cell Death. Cell Rep. *12*, 673–683.

Maas, S.L.N., Breakefield, X.O., and Weaver, A.M. (2017). Extracellular Vesicles: Unique Intercellular Delivery Vehicles. Trends Cell Biol. *27*, 172–188.

Malinova, T.S., and Huveneers, S. (2018). Sensing of Cytoskeletal Forces by Asymmetric Adherens Junctions. Trends Cell Biol. *28*, 328–341.

McCann, A.P., Scott, C.J., Van Schaeybroeck, S., and Burrows, J.F. (2016). Deubiquitylating enzymes in receptor endocytosis and trafficking. Biochem. J. *473*, 4507–4525.

Neefjes, J., Jongsma, M.M.L., and Berlin, I. (2017). Stop or Go? Endosome Positioning in the Establishment of Compartment Architecture, Dynamics, and Function. Trends Cell Biol. *27*, 580–594.

Paul, N.R., Jacquemet, G., and Caswell, P.T. (2015). Endocytic Trafficking of Integrins in Cell Migration. Curr. Biol. *25*, R1092–R1105.

Phillips, M.J., and Voeltz, G.K. (2016). Structure and function of ER membrane contact sites with other organelles. Nat. Rev. Mol. Cell Biol. *17*, 69–82.

Pickart, C.M. (2001). Mechanisms underlying ubiquitination. Annu. Rev. Biochem. *70*, 503–533.

Polo, S. (2012). Signaling-mediated control of ubiquitin ligases in endocytosis. BMC Biol. *10*, 25.

Qin, Y., Zhou, M.T., Hu, M.M., Hu, Y.H., Zhang, J., Guo, L., Zhong, B., and Shu, H.B.) (2014). RNF26 temporally regulates virus-triggered type I interferon induction by two distinct mechanisms. PLoS Pathog. *10*, e1004358.

Raiborg, C., and Stenmark, H. (2009). The ESCRT machinery in endosomal sorting of ubiquitylated membrane proteins. Nature *458*, 445–452.

Raiborg, C., Wenzel, E.M., Pedersen, N.M., Olsvik, H., Schink, K.O., Schultz, S.W., Vietri, M., Nisi, V., Bucci, C., Brech, A., et al. (2015a). Repeated ER-endosome contacts promote endosome translocation and neurite outgrowth. Nature *520*, 234–238.

Raiborg, C., Wenzel, E.M., and Stenmark, H. (2015b). ER-endosome contact sites: molecular compositions and functions. EMBO J. *34*, 1848–1858.

Rocha, N., Kuijl, C., van der Kant, R., Janssen, L., Houben, D., Janssen, H., Zwart, W., and Neefjes, J. (2009). Cholesterol sensor ORP1L contacts the ER protein VAP to control Rab7-RILP-p150 Glued and late endosome positioning. J. Cell Biol. *185*, 1209–1225.

Rowland, A.A., Chitwood, P.J., Phillips, M.J., and Voeltz, G.K. (2014). ER contact sites define the position and timing of endosome fission. Cell *159*, 1027–1041.

Sapmaz, A., Berlin, I., Bos, E., Wijdeven, R.H., Janssen, H., Konietzny, R., Akkermans, J.J., Erson-Bensan, A.E., Koning, R.I., Kessler, B.M., et al. (2019). USP32 regulates late endosomal transport and recycling through deubiquitylation of Rab7. Nat. Commun. *10*, 1454.

Schindelin, J., Arganda-Carreras, I., Frise, E., Kaynig, V., Longair, M., Pietzsch, T., Preibisch, S., Rueden, C., Saalfeld, S., Schmid, B., et al. (2012). Fiji: an open-source platform for biological-image analysis. Nat. Methods *9*, 676–682.

Shevchenko, A., Tomas, H., Havlis, J., Olsen, J.V., and Mann, M. (2006). In-gel digestion for mass spectrometric characterization of proteins and proteomes. Nat. Protoc. *1*, 2856–2860.

Stewart, M.D., Ritterhoff, T., Klevit, R.E., and Brzovic, P.S. (2016). E2 enzymes: more than just middle men. Cell Res. *26*, 423–440.

Sugiyama, M.G., Fairn, G.D., and Antonescu, C.N. (2019). Akt-ing Up Just About Everywhere: Compartment-Specific Akt Activation and Function in Receptor Tyrosine Kinase Signaling. Front. Cell Dev. Biol. *7*, 70.

Taguchi, T., and Mukai, K. (2019). Innate immunity signalling and membrane trafficking. Curr. Opin. Cell Biol. *59*, 1–7.

Tiwari, S., and Weissman, A.M. (2001). Endoplasmic reticulum (ER)-associated degradation of T cell receptor subunits. Involvement of ER-associated ubiquitin-conjugating enzymes (E2s). J. Biol. Chem. *276*, 16193–16200.

van de Weijer, M.L., Bassik, M.C., Luteijn, R.D., Voorburg, C.M., Lohuis, M.A., Kremmer, E., Hoeben, R.C., LeProust, E.M., Chen, S., Hoelen, H., et al. (2014). A high-coverage shRNA screen identifies TMEM129 as an E3 ligase involved in ER-associated protein degradation. Nat. Commun. *5*, 3832.

van de Weijer, M.L., Schuren, A.B.C., van den Boomen, D.J.H., Mulder, A., Claas, F.H.J., Lehner, P.J., Lebbink, R.J., and Wiertz, E.J.H.J. (2017). Multiple E2 ubiquitin-conjugating enzymes regulate human cytomegalovirus US2-mediated immunoreceptor downregulation. J. Cell Sci. *130*, 2883–2892.

van der Kant, R., Fish, A., Janssen, L., Janssen, H., Krom, S., Ho, N., Brummelkamp, T., Carette, J., Rocha, N., and Neefjes, J. (2013). Late endosomal transport and tethering are coupled processes controlled by RILP and the cholesterol sensor ORP1L. J. Cell Sci. *126*, 3462–3474.

Vennegoor, C., and Rümke, P. (1986). Circulating melanoma-associated antigen detected by monoclonal antibody NKI/C-3. Cancer Immunol. Immunother. *23*, 93–100.

Wang, X., Herr, R.A., Rabelink, M., Hoeben, R.C., Wiertz, E.J., and Hansen, T.H.) (2009). Ube2j2 ubiquitinates hydroxylated amino acids on ER-associated degradation substrates. J. Cell Biol. *187*, 655–668.

Weber, A., Cohen, I., Popp, O., Dittmar, G., Reiss, Y., Sommer, T., Ravid, T., and Jarosch, E. (2016). Sequential Poly-ubiquitylation by Specialized Conjugating Enzymes Expands the Versatility of a Quality Control Ubiquitin Ligase. Mol. Cell *63*, 827–839.

Wijdeven, R.H., Janssen, H., Nahidiazar, L., Janssen, L., Jalink, K., Berlin, I., and Neefjes, J. (2016). Cholesterol and ORP1L-mediated ER contact sites control autophagosome transport and fusion with the endocytic pathway. Nat. Commun. *7*, 11808.

Wong, L.H., Gatta, A.T., and Levine, T.P. (2019). Lipid transfer proteins: the lipid commute via shuttles, bridges and tubes. Nat. Rev. Mol. Cell Biol. *20*, 85–101.

Yang, M., Ellenberg, J., Bonifacino, J.S., and Weissman, A.M. (1997). The transmembrane domain of a carboxyl-terminal anchored protein determines localization to the endoplasmic reticulum. J. Biol. Chem. *272*, 1970–1975.

Zheng, N., and Shabek, N. (2017). Ubiquitin Ligases: Structure, Function, and Regulation. Annu. Rev. Biochem. *86*, 129–157.

Zickermann, V., Angerer, H., Ding, M.G., Nübel, E., and Brandt, U. (2010). Small single transmembrane domain (STMD) proteins organize the hydrophobic subunits of large membrane protein complexes. FEBS Lett. *584*, 2516–2525.

STAR★METHODS

KEY RESOURCES TABLE

REAGENT or RESOURCE	SOURCE	IDENTIFIER
Antibodies		
mouse anti-HA 16B12	Covance	Cat# #MMS-101P; RRID: AB_2314672
rabbit anti-GFP	Rocha et al., 2009	N/A
rabbit anti-RFP	Rocha et al., 2009	N/A
mouse anti-RFP 6G6	Chromotek	Lot#51020014AB-01; RRID: AB_2631395
rabbit anti-EGFR	Millipore	Cat# 06-847; Lot# 3016636; RRID:AB_2096607
mouse anti-actin AC15	Sigma	Cat#A5441d; RRID: AB_476744
mouse anti-phosphotyrosine pY 4G10	Millipore	Cat# 05-321; Lot#3105748; RRID:AB_309678
Rabbit anti-AKT (pan)	Cell signaling	Cat# 9272; RRID:AB_329827
Rabbit anti-AKT T308	Cell signaling	Cat# C31E5E; Lot#18 10/2018; RRID:AB_2202760)
Rabbit anti-AKT S473	Cell signaling	Cat# 4060; Lot# 24 11/2018
Mouse anti-Vinculin	Sigma	Cat# V9131; Lot#079M4754V; RRID:AB_477629
Mouse anti-UBE2J1	Santa Cruz	Cat# Sc-377002; Lot#F1412
goat anti-mouse-HRP	Invitrogen	Cat# G21040; Lot#2122350; RRID:AB_2536527
goat anti-rabbit-HRP	Invitrogen	Cat# G21234; Lot#215643; RRID:AB_2536530
goat anti-rabbit IRdye800	Li-Cor	Cat# 926/68070; Lot# C80307-05; RRID: AB_621843
goat anti-mouse IRdye680	Li-Cor	Cat# 926-32211; Lot# C91211-03
mouse anti-EEA1	BD transduction laboratories	Cat# 610457; RRID:AB_397830
mouse anti-CD63	Vennegoor and Rümke, 1986	NKI-C3
mouse anti-M6PR	Abcam	Cat# ab2733; RRID:AB_2122792
mouse anti-TfR	Invitrogen	Cat# 905963A
mouse anti-Ubiquitin	Santa Cruz	sc-8017; Lot#D0115; RRID:AB_2762364
rabbit anti-LAMP1	Sino Biolocial	11215-R107; RRID:AB_2860324
rabbit anti-VAP-A	Proteintech	15275-1-AP; Lot# 00022782; RRID: AB_2256991
rat anti-HA (3F10)	Roche	11867423001; Lot# 34502100; RRID:AB_390918
donkey anti-mouse Alexa488	invitrogen	A21202; Lot#1915874; RRID:AB_141607
donkey anti-mouse Alexa568	invitrogen	A10037; Lot#1917938; RRID:AB_2534013
donkey anti-mouse Alexa647	invitrogen	A31571; Lot#1900251; RRID: AB_162542
donkey anti-rabbit Alexa488	invitrogen	A21206; Lot#1981155; RRID:AB_2535792
donkey anti-rabbit Alexa568	invitrogen	A10042; Lot#1891789; RRID:AB_2534017
donkey anti-rabbit Alexa647	invitrogen	A31573; Lot#1964354; RRID: AB_2536183
donkey anti-rat DyLight 650	Invitrogen	SA510029; Lot# 2K2477302; RRID:AB_2556609
Anti-Rabbit, IgG, HRP	Thermo Fischer	Cat#G-21234; RRID: AB_1500696
Anti-Mouse, IgG, HRP	Thermo Fischer	Cat#G-21040; RRID: AB_2536527
PE-coupled anti-EGFR	BD	555997; Lot#84901; RRID: AB_396281
Chemicals, peptides, and recombinant proteins		
Alexa647-coupled recombinant EGF	Invitrogen	E35351; Lot#1975019
EGF	Berlin et al., 2010	N/A
LysoTracker Far-Red	Invitrogen	L12492; Lot# 1843533
LysoSensor Green	Invitrogen	L7535; Lot#2145058
DMNG	Anatrace	Lot# 4217219
X-treme GENE HP DNA Transfection Reagent	Roche	Cat#6366244001
cOmplete Protease Inhibitor Cocktail	Roche	Cat#11697498001
SuperSignal West Dura Extended Duration Substrate	ThermoFisher	Cat#34076
GFP-TRAP beads	Chromotek	Lot#80529001A

(Continued on next page)

Continued

REAGENT or RESOURCE	SOURCE	IDENTIFIER
RFP-TRAP beads	Chromotek	Lot#70227002A
DharmaFECT-1	Dharmacon	Cat#T-2001-03
Deposited data		
Raw gel scans	Mendeley	https://doi.org/10.17632/nn9ryfpy7h.1
Mass-spectrometry spectra	PRIDE	PXD022104
Experimental models: cell lines		
HeLa	ATCC	CCL-2
MJS	Prof. G. Riethmuller	LMU, Munich
HEK293T	ATCC	CRL-3216
Oligonucleotides		
siRNF26-1 (GAGAGGAUGUCAUGCGGCU)	Dharmacon	siGENOME D-007060-17
siUBE2J1-1 (GGCUAAUGGUCGAUUUGAA)	Dharmacon	siGENOME D-007266-20
siUBE2J1-2 (GAAUAUAUCUGGCAAACGA)	Dharmacon	siGENOME D-007266-3
siUBE2J1-3 (GAAAGAAGCGGCAGAAUUG)	Dharmacon	siGENOME D-007266-1
J1 KO gRNA GGGTCTCCATGGTGGGTCGC	van de Weijer et al., 2017	N/A
siUBE2J2-pool	Dharmacon	M-008614-02-0005
Recombinant DNA		
pDEST17-UBE2J2	Addgene	Addgene#15794
UBE2J2-C93S	E. Wiertz, Utrecht	N/A
HA-Ubiquitin	I. Dikic, Frankfurt	N/A
GFP-EPS15	O. Bakke, Oslo	N/A
pX459V2	Zhang lab, Standford	Addgene#62988
RFP-RNF26	Jongsma et al., 2016	N/A
RFP-RNF26 dRING	Jongsma et al., 2016	N/A
RFP-RNF26 I382R	Jongsma et al., 2016	N/A
GFP-UBE2J1	This study	N/A
GFP-UBE2J1 1-282 (ΔTMD)	This study	N/A
GFP-UBE2J1 284-318 (TMD)	This study	N/A
RFP-UBE2J1 C91A	This study	N/A
RFP-UBE2J2	This study	N/A
GFP-UBE2J2	This study	N/A
RFP-UBE2J2 C93S	This study	N/A
GFP-UBE2J2 C93S	This study	N/A
RFP-UBE2J1 1-283-(UBE2J2 272-259) (J1(J2TMD))	This study	N/A
GFP-MOSPD2(TMD)	Cabukusta et al., 2020	N/A
RFP-UBE2J1 1-283-(MOSPD2 497-518) (J1(MSD2TMD))	This study	N/A
GFP-SQSTM1	Jongsma et al., 2016	N/A
HA-SQSTM1	Jongsma et al., 2016	N/A
RFP-TOLLIP	Jongsma et al., 2016	N/A
GFP-TOLLIP	Jongsma et al., 2016	N/A
GFP-EPS15	Jongsma et al., 2016	N/A
Software and algorithms		
ImageJ	Schindelin et al., 2012	https://imagej.nih.gov/ij/
LasX	Leica	N/A
Image Studio	Li-Cor	N/A
Imaris	Oxford Instruments	N/A
maxQuant	Cox and Mann, 2008	https://www.maxquant.org/

RESOURCE AVAILABILITY

Lead contact
Further information and requests for resources and reagents should be directed to and will be fulfilled by the Lead Contact, Ilana Berlin (I.Berlin@lumc.nl).

Materials availability
All plasmids generated in this study are available from the lead contact upon request.

Data and code availability
The mass spectrometry proteomics data have been deposited to the ProteomeXchange Consortium via the PRIDE partner repository with the dataset identifier PRIDE: PXD022104.

Raw scans are available via Mendeley Data (https://doi.org/10.17632/nn9ryfpy7h.1).

EXPERIMENTAL MODEL AND SUBJECT DETAILS

Cell lines
MelJuSo cells (female, human melanoma), kindly provided by Prof. G. Riethmuller (LMU, Munich), were cultured in Iscove's modified Dulbecco's medium (IMDM) medium (GIBCO). HeLa cells (female, CCL-2), and HEK293T cells (female) were type-verified and cultured in DMEM medium (GIBCO). All media were supplemented with 8% fetal calf serum (FCS, Sigma). All cell lines were cultured at 37°C and 5% CO_2 and routinely tested (negatively) for mycoplasma.

METHOD DETAILS

siRNA transfections
For the initial E2 screen, pooled siRNAs were bought from Dharmacon (siGenome (M) series). Sequences of the siRNA oligos targeting RNF26 and UBE2J1, bought from Dharmacon, are shown in the Key resources table. For RNF26 silencing, we used siRNF26-1. For UBE2J1 silencing, we used a pool of all three siRNAs unless stated otherwise in figure legends. Gene silencing was performed in a 48 or 24 well plate (IF) or 12 well plate (WB) - reagent volumes were scaled up accordingly. In a 48 well plate, 25-32.5μL siRNA (for sequences, see Key resources table) was mixed with 25uL 1x siRNA buffer (GE Healthcare) containing 0.5uL Dharmafect 1 transfection reagent. The mix was incubated on a shaker at RT for 40 minutes before the addition of 7.000 HeLa or MelJuSo cells (and coverslips). Cells were cultured for three days before analysis. Non-targeting siRNA or reagent only was used as a negative control. UBE2J2 was silenced using siRNAs from the siGenome SMARTpool library (Dharmacon).

Constructs
RNF26 (and mutants), SQSTM1 and TOLLIP constructs, all expressed from C1/N1 vector series (Clontech), as well as HA-Ubiquitin and GFP-EPS15 constructs have been previously described (Jongsma et al., 2016). UBE2J1 (or UBE2J2) was subcloned between XhoI (or EcoRI) and BamHI sites of the C1-RFP and C1-GFP vector (Clontech). UBE2J1 truncations and mutants were created by standard (mutagenesis) PCR methods. UBE2J1(MSD2TMD) and UBE2J1(J2TMD) were created by fusing the cytoplasmic tail (aa1-282) of UBE2J1 to the TMD of MOSPD2 or UBE2J2 using NEBuilder HiFi DNA Assembly (NEB).

DNA transfections
Cells were seeded in culture plates to reach approx. 70% confluency on the day of transfection. HeLa were transfected with Effectene (QIAGEN) (200ng DNA per well of 24 well plate), according to the manufacturer's protocol. MelJuSo cells were transfected using Extremegene HP (Roche) (500ng DNA per well in 24 well plate), according to manufacturer's protocol. Cells were cultured overnight before analysis. HEK293 cells were transfected with PEI at a ratio of 3μg PEI per μg DNA in 200μL DMEM medium. After 15-30 min, the mix was added dropwise to the cells which were then cultured overnight before analysis.

CRISPR/Cas9-mediated knockout
gRNA sequences targeting the UBE2J1 gene (see Key resources table) were cloned into the BbsI site of PX459V2 (containing the Cas9 gene and a puromycin resistance gene). This plasmid was transfected into HeLa cells and the next day, cells were selected with 200ug/mL puromycin for 3 days. Then, cells were diluted and cultured in a 15cm dish, allowing well separates colonies to grow. These were isolated, expanded, and analyzed for loss of UBE2J1 by western blot.

EGFR degradation
Ligand-mediated turnover was assayed as previously described (Berlin et al., 2010) using 100 ng/mL EGF. Receptor levels were quantified at each time point relative to actin levels and expressed as a fraction of EGFR at t = 0 min. Receptor activation and downstream signaling was expressed relative to the maximum activation (t = 5 min).

Immunofluorescence confocal microscopy

Cells grown on coverslips (Menzel Gläser) were fixed with 3.7% paraformaldehyde, washed three times with PBS, permeabilized with 0.1%TX100 for 10 min and blocked in 0.5% BSA for one hour. Next, coverslips were incubated with primary antibodies in 0.5% BSA for 1hr at RT, washed and incubated with Alexa-labeled anti mouse/rabbit/rat secondary antibody or streptavidin. After washing, coverslips were mounted on glass slides with ProLong Gold with DAPI (Life Technologies). Samples were imaged with a Leica SP8 confocal microscope equipped with appropriate solid-state lasers, HCX PL 63 times magnification oil emersion objectives and HyD detectors (Leica Microsystems, Wetzlar, Germany). Data was collected using 2048 × 2048 scanning format with line avering without digital zoom, or 1024 × 1024 scanning format with digital zoom in the range of 1.0-2.0 with line averaging. Images were smoothened with 1 pixel average filter in ImageJ. Quantification of endosome positioning was performed as previously described with minor alterations (Jongsma et al., 2016; Sapmaz et al., 2019). In short, fluorescence intensities (above automated background threshold) were measured along a straight line ROI (regions of interest) drawn from the border of a cell's nucleus (fractional distance = 0) to the plasma membrane (fractional distance = 1.0) using the line profile tool in the LAS-AF software, and their absolute distance to the border of the nucleus was expressed relative to the total length of the line. Fractional distances are reported in scatterplots along with the mean distance value (red line) within the sample and the total number of cells analyzed.

Live microscopy

For live microscopy, cells were seeded in 4-chamber live cell dishes and imaged under conditions of 37°C and 5% CO2 with a Leica SP8 confocal microscope equipped with wide light lasers. Data was collected using 63x oil immersion objectives and 1.5x magnification in a 1024 × 1024 scanning format at 0.58 frames/sec with line averaging. Tracking of lysotracker-positive vesicles in manually selected cells was performed using TrackMate for FiJi. FiJi was also used for post-collection image processing.

For hypotonic shock experiments (Figures 5A and S3B), cells were incubated in mQ + 5% DMEM for 10 minutes before imaging on a Leica SP8 with Andor Dragonfly spinning disc module. 0,2μM Z stacks were acquired with a 100x oil immersion objective and processed with Imaris software for 3D rendering.

Co-immunoprecipitations

HEK293T cells were lysed in 1% DMNG buffer (150mM NaCl, 50mM Tris-HCl pH 7.5, 5mM MgCl$_2$, 1% DMNG, protease inhibitors (Roche diagnostics, EDTA free) for 90 min, rotating at 4°C. After 15 min 20,000x g centrifugation, post-nuclear lysates were incubated with GFP-TRAP beads (Chromotek) and rotated for 90 min at 4°C before subsequent immunoisolation with RFP-TRAP beads to acquire input samples. Beads were washed four times in 0.2% DMNG lysis buffer. Samples were boiled for 10 min in 2x Laemmli buffer prior to analyses by SDS-PAGE and western blotting.

Ubiquitylation assays

HEK293T cells were lysed in 0.5% TX-100 lysis buffer (150mM NaCl, 50mM Tris-HCl pH 7.5, 5mM MgCl$_2$, 0.5% (v/v) TX-100 and protease inhibitors (Roche diagnostics, EDTA free)). Nuclei were lysed by adding 1:4 SDS buffer (2% SDS, EDTA) and samples were sonicated (5x1s pulses, 80% power, Fisher Scientific). Samples were diluted to 0.2% SDS with TX-100 lysis buffer and centrifuged for 20 min at 20,000 x g. After spinning, samples were incubated with GFP-TRAP beads (Chromotek) for 3hrs at 4°C. Beads were washed 4 times with 1% SDS in PBS before elution in 2x Laemmli sample buffer by boiling for 10 min.

SDS-PAGE and western blotting

Samples were separated by 8% (ubiquitination assays) or 10/12% (regular lysates, CoIPs) SDS-PAGE and transferred to nitrocellulose or PVDF membranes in ethanol-containing transfer buffer at 300mA for 2-3 h. The membranes were blocked with 5% milk/PBS before incubation with primary antibody diluted in blocking buffer for 1hr at RT. After washing twice with PBS/0.1% Tween-20, proteins were detected with secondary antibodies. Depending on the secondary antibody, detections were performed by incubation with ECL reagent (SuperSignal West Dura Extended Duration, GE Healthcare) or directly imaged with an Odyssey Fx laser scanning fluorescence imager.

Flow cytometry

For quantification of intracellular acidity, MJS cells were trypsinyzed, suspended in pre-heated growth medium and incubated for 5 minutes with 2,5 μM LysoSensor Green at 37°C before two cold washes with FACS buffer (2% FCS in PBS) and storage on ice until analysis. For detection of cell surface EGFR, HeLa cells were trypsinized, suspended in FACS buffer and stained with PE-conjugated anti-EGFR for 30 min on ice. After two washes with ice-cold FACS buffer, cells were fixed in FACS buffer containing 0.1% PFA until analysis. Data was analyzed on a FACS Calibur flow cytometer (BD Biosciences) and quantified using FlowJo software.

In-gel digestion

HA pulldown samples were fractionated for 15 min at 150V on a 4%–12% Bis-Tris gradient gel using MOPS buffer. Entire lanes were processed by in-gel digestion according to a previously published protocol (Shevchenko et al., 2006).

Mass spectrometry

Samples were processed on a EASY-nLC 1000 system (Proxeon, Odense, Denmark) connected to a Q-Exactive Orbitrap (Thermo Fisher Scientific, Bremen, Germany) through a nano-electrospray ion source. Peptides were fractionated by chromatography using a column with 360 μm OD, 75 μm ID, 15 μm tip ID, non-coated, 25 cm length (MS Wil, Aarle-Rixtel, Netherlands); in-house packed with 1.8 μm C18 beads (Reprospher-DE, Pur, Dr.Manish, Ammerbuch-Entringen, Germany). Peptides were fractionated on a 120 min solvent gradient from 2% to 95% acetonitrile in 0.1% formic acid at a flow rate of 200nL/minute. The mass spectrometer was operated in data-dependent acquisition mode with a top 10 method. Full-scan MS spectra were acquired at a target value of 3×10^6 and a resolution of 70,000, and the higher-collisional dissociation (HCD) tandem mass spectra (MS/MS) were recorded at a target value of 1×10^5 with a resolution of 17,500 using a normalized collision energy (NCE) of 25%. The maximum MS1 and MS2 injection times were 20 ms and 60 ms, respectively. The precursor ion masses of scanned ions were dynamically excluded (DE) from MS/MS analysis for 60 s. Ions with charge 1, and greater than 6 were excluded from triggering MS2 events.

MS data analysis

MS data files were analyzed using MaxQuant (version 1.6.14) matching to a Uniprot Human Proteome (Uniprot filtered reviewed *H. sapiens* proteome downloaded June 22 2020) and a custom FASTA sequence of 2xHA-SQSTM1 with default settings for FDR and andromeda score filtering, matching to a decoy database and common contaminants. Digestion was set to allow 4 missed cleavages with Trypsin digestion. Normalization was done by LFQ (default settings) with matching between runs enabled. Cysteine carbamidomethylation was set as fixed modification and N-terminal acetylation, oxidation of methionine, phosphorylation (S,T and Y) and GlyGly modification on Lysine were included as variable modifications. Intensity data was plotted from GlyGly (K)Sites.txt output files.

QUANTIFICATION AND STATISTICAL ANALYSIS

Details for statistical analysis can be found in the figure legends. For IF experiments, multiple cells from at least two experiments were included in quantification. Gel experiments were repeated at least three times of which a representative scan is shown. Quantification figures show each single data point with mean ± standard deviation. Western blots were quantified with Li-Cor Image studio software with automatic background correction. Statistical analysis was performed with two-tailed Students' t test.